Digest Journal of Nanomaterials and Biostructures Vol. 19, No. 4, October-December 2024, p. 1633-1644

Sol-gel preparation and visible-light-driven photocatalytic activity of the double perovskite Sr_2FeMoO_6

L. Y. Zhang[a,*], Y. Gao[a], G. H. Zheng[b], Q. Wang[a], Z. Z. Xu[a]
[a]*School of Energy Materials and Chemical Engineering, Hefei University, Hefei 230601, China*
[b]*School of Material Science and Engineering, Anhui University, Hefei 230039, China*

Sr_2FeMoO_6 was synthesized as a visible-light-driven photocatalytic double perovskite by a simple sol-gel preparation method. In-depth experimental techniques were used to characterize morphological and optical properties. Scanning and transmission electron microscopy revealed a tubular shape morphology, resulting in a large active surface area for improved photocatalysis. Optimization of Sr_2FeMoO_6 achieved a narrow bandgap of 1.77 eV, capable of interacting with visible light. The decomposition of methylene blue (MB) under visible-light irradiation was employed to assess the photocatalytic performance of as-synthesized samples.The Sr_2FeMoO_6 samples exhibited excellent degradation performance, demonstrating a 95.6% degradation of MB within 35 min of irradiation. This work has certain research significance by revealing the potential mechanism of double perovskite photocatalysts.

(Received August 22, 2024; Accepted October 25, 2024)

Keywords: Sr_2FeMoO_6, Sol-gel method, Synthesis, Photocatalysis

1. Introduction

Double perovskite-like compounds with $A_2BB'O_6$ structures (A: rare earth/alkaline earth cation; B: transition metal; B': transition metal) have recently been the focus of discussion due to their unique structure and superior properties. This class of materials exhibits promising carrier transport abilities and magnetic, multiferroic, and optoelectronic properties, which make them suitable for different applications [1-5]. In particular, an increasing number of $A_2BB'O_6$ materials with promising photocatalytic properties have been reported. For example, A_2NiWO_6 (A: Ca, Sr) compounds have shown excellent photocatalytic activities for the degradation of organic molecules [6]. The improved catalytic performance of the $A_2BB'O_6$ compounds has been ascribed to their atomic structure. Specifically, it has been found that the BO_6 octahedron structure of perovskite-type oxides facilitates the creation of electron transition and oxygen vacancies in the process of photocatalysis [7-10].

Among the many double perovskite oxides, Sr_2FeMoO_6 has superior magnetic characteristics and resistivity properties for spintronic and magneto-resistive applications. The

*Corresponding author: lingyunf@126.com
https://doi.org/10.15251/DJNB.2024.194.1633

crystalline architecture of the double perovskite exhibits a sophisticated composition, featuring two interpreting face-centered cubic sublattices. The rare earth/alkaline earth ion A is Sr, and the 3d transition metal ion B is Fe while the 4d/5d transition metal ion B' is Mo, arranged in a rock-salt crystal structure [11]. The construction of the double perovskite structure involves the sharing of corners between FeO_6 and MoO_6 octahedra. Additionally, this material is optically active and can promote the generation of photo-induced electrons by enabling transitions from O2p orbitals to empty Fe3d levels. Furthermore, the photoluminescent properties are measured and demonstrated that the photogenerated charge carriers exhibit a reduced recombination rate after excitation, enabling the separated electrons and holes to engage in reactions with dye molecules more effectively. Furthermore, the $3d^64s^2$ electronic configuration of Fe^{3+} ions is advantageous for enhancing photocatalytic degradation. They can split into local energy levels coordinating with other ions, and the band energy can be greatly reduced. As a result, charge-transfer transitions can be enhanced, and photocatalysis can be driven by visible light. This conclusion has been confirmed in the study of Fe^{3+}-doped photocatalysts [12]. In addition, the concurrent presence of Mo^{6+} and Fe^{3+} ions within the B and B' sites of perovskite induces significant energy hybridizations and lattice distortions. This structure is particularly advantageous for promoting charge separation and enhancing photocatalytic efficiency when exposed to visible light.

Here, Sr_2FeMoO_6 compounds were prepared by an improved citric-acid sol-gel method, and their photocatalytic performance toward the degradation of methylene blue (MB) was determined and discussed. To the best of our knowledge, no such comprehensive study has been performed. X-ray diffraction (XRD), Raman spectroscopy, scanning electron microscopy (SEM), high-resolution transmission electron microscopy (HRTEM), N_2 adsorption-desorption isotherm investigations, UV-vis diffuse reflectance spectroscopy, and photocatalytic measurements were employed to study the structure, morphology, optical properties, and photocatalytic activities. The used synthesis method resulted in Sr_2FeMoO_6 compounds with a tubular shape morphology and an increased surface area as a consequence, which is beneficial for photocatalysis. The UV-vis diffuse reflectance spectroscopy results indicated for Sr_2FeMoO_6 a bandgap of about 1.77 eV, which suggests that it can absorb visible light well. MB solutions were degraded nearly 95.6% within 35 min of irradiation.

2. Experimental

2.1. Synthesis of materials

Sr_2FeMoO_6 was synthesized via a chemical sol-gel route. Stoichiometric amounts of the reactants $(NH_4)_6Mo_7O_{24}\cdot 4H_2O$ and $Sr(NO_3)_2$ were each dissolved in deionized water. The corresponding amount of $Fe(NO_3)_3$ was dissolved in an aqueous citric acid solution. Then, the three solutions were combined under vigorous stirring. A certain amount of citric acid was added to the liquid, and the pH of the mixture was adjusted to 7.0 by adding ammonia solution. The mixed solution was agitated in a water bath and aged to form a transparent red gel, which was subsequently dehydrated in an oven. The obtained powder was pressed and then heated at 1150 ℃ in a flow of a gas mixture of 5□ H_2 in N_2 to finally obtain double perovskite Sr_2FeMoO_6 photocatalyst.

2.2. Characterization

The calcination temperature of the precursor was determined by thermal analysis with a thermogravimetric analyzer (TGA; Q500, TA, USA). The crystalline properties of the samples were examined by XRD with an X-ray diffractometer (DX-2000, Rigaku, Japan), employing Cu $K\alpha$ radiation with a wavelength of λ = 1.5408 Å over a scan range of 10-80º with steps of 0.02º. Raman spectroscopy was carried out with the DXR confocal microscopic Raman spectrometer of Thermo Fisher Scientific (USA). The morphology and dimensions of the samples were characterized by field-emission SEM (SU8010, Hitachi, Japan) and HRTEM (JEM-2100, JEOL, Japan). Elemental compositions were determined by energy-dispersive X-ray spectroscopy (EDS; SU8010, Hitachi, Japan). An automatic specific surface analyzer (Autosorb-iQ, Quantachrome, USA) was employed to record N_2 adsorption-desorption isotherms of the samples at 77.3 K and analyze the data to obtaintheir surface area according to the Brunauer-Emmett-Teller (BET) theory. Optical diffuse reflectance spectra were obtained by ultraviolet-visible (UV-vis) diffuse reflectance spectroscopy (V-6500, Jasco, Japan). Electron spin resonance (ESR) analyses were conducted at room temperature utilizing a continuous-wave X-band ESR spectrometer (EMX plus 10/12, Bruker, Germany). In the experiment, radicals were trapped through scavenging agents such as 5, 5-dimethyl-1-pyrroline N-oxide (DMPO).

2.3. Photocatalytic activity

Visible-light degradation (300W Xe lamp) of MB was used to evaluate the photocatalytic performance of Sr_2FeMoO_6. Briefly, 0.15 g photocatalyst was dispersed into 100 mL of a 4.2×10^{-5}-M MB solution. First, the reaction mixture was magnetically stirred for 1.0 h in the dark to establish the adsorption-desorption equilibrium of the photocatalyst and MB. Thereafter, the suspension was subjected to illumination by the Xe lamp. At regular time intervals, the suspensions were sampled, and the photocatalyst was removed by centrifugation before the spectrophotometric determination of the MB concentrations in the supernatant over the course of the photodegradation.

3. Results and discussion

3.1. TG analysis

Figure 1 displays the thermogravimetric analysis (TGA) results of the Sr_2FeMoO_6 precursor. The temperature was raised from room temperature to 800 ℃, and within this range, the TGA curve presents four peaks associated with mass loss. The first peak was observed between 50 and 150 ℃ and refers to the loss of water absorbed on the surface. The following peak at 205 ℃ was attributed to the carbonization of the chelating agent citric acid. The third weight loss occurred between 320 and 375 ℃ and was associated with the decomposition of residual nitrate and the crystallization of $SrMoO_4$. The last peak was observed at 695 ℃, related to the decomposition of residual carbon and some $SrFeO_{3-x}$ crystallization. Due to instrumentation limits, the crystallization process could not be monitored above 800 °C. However, previous literature demonstrated that weight change over 800 °C is not significant [13, 14].

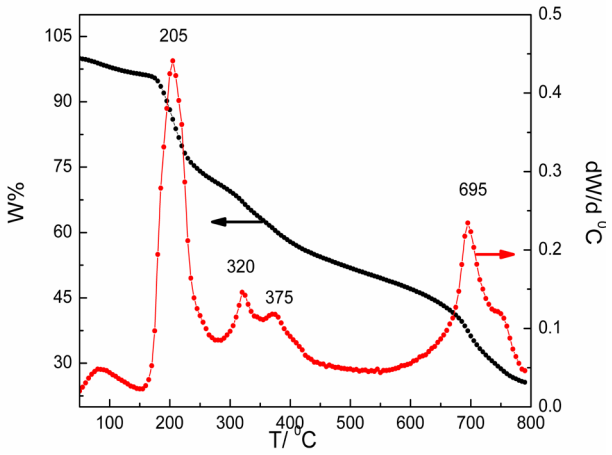

Fig.1. Thermogravimetric analysis curve of Sr_2FeMoO_6 precursor.

3.2. XRD analysis

The phase purity and crystallinity of Sr_2FeMoO_6 samples were examined by XRD (Figure 2). The spectrum showed several intense peaks which were indexed as pure tetragonal structures (I4/mmm space group) in good agreement with the standard card (JCPDS70-4088). It is worth noting that in addition to the main peak of Sr_2FeMoO_6, the XRD pattern also contained Bragg peaks corresponding to secondary $SrMoO_4$. The occurrence of $SrMoO_4$ may be attributed to the insufficient reduction of the precursor, which was also deduced from the Raman analysis shown below [15].

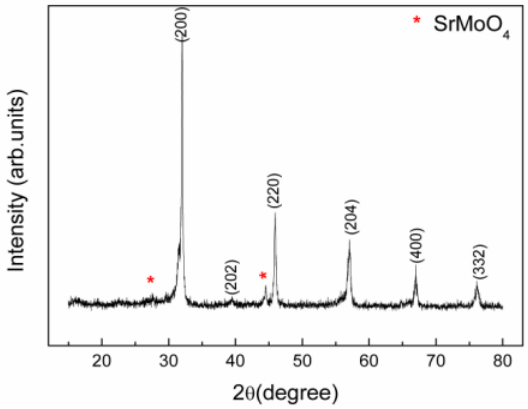

Fig.2. XRD patterns of Sr_2FeMoO_6 sample.

3.3.Raman analysis

Figure 3 displays the Raman spectra of Sr_2FeMoO_6, presenting multiple characteristic Raman peaks. The peaks at 210, 295, 390, 440, 620, and 770 cm^{-1} were attributed to the Sr_2FeMoO_6 phase, while those at 360, 840, and 880 cm^{-1} were ascribed to MoO_4 group vibrations, suggesting the presence of $SrMoO_4$ impurities [16, 17]. The other peaks at 320 and 520 cm^{-1} may originate from $SrFeO_{3-x}$ [18].

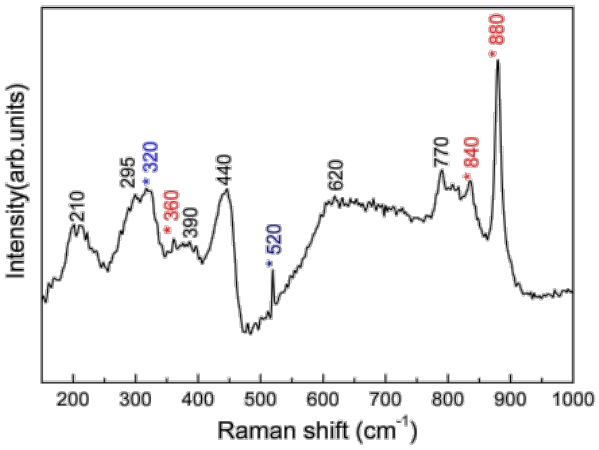

Fig.3. Raman spectra of Sr_2FeMoO_6 sample.

3.4. SEM analysis

To examine the morphological characteristics of the samples, SEM was performed on the Sr_2FeMoO_6 samples (Figure 4(a,b)). Under the used sol-gel protocol, the morphology of the sample exhibited a tubular shape with an estimated width and length of approximately 50 nm and 5 μm, respectively. Figure 4(c,d) shows the EDS spectra to detect the elements present in Sr_2FeMoO_6. The spectrum revealed multiple prominent peaks attributed to Sr, Fe, Mo, and O.

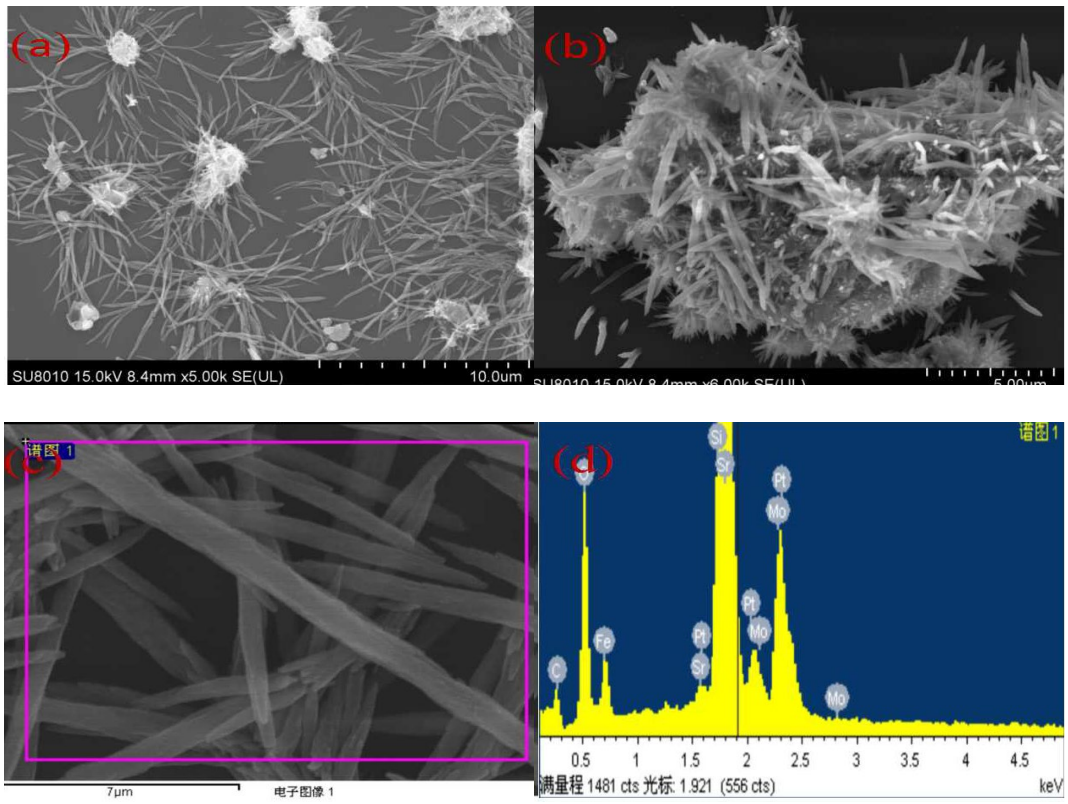

Fig.4. SEM images (a-b) and EDS spectra (c-d) of Sr_2FeMoO_6 sample.

3.5. TEM analysis

In addition, TEM was employed for the in-depth morphology investigation of tubular-shaped Sr_2FeMoO_6. Figure 5(a,b) shows typical TEM and HRTEM results of thissample and indicates that the tubular shape of the Sr_2FeMoO_6 samples was assembled by layering hundreds of nanorods with lengths ranging from 250 to 800 nm and diameters of approximately 50 to 150 nm. In agreement with the XRD results (Figure 2), the selected area electron diffraction (SAED) patterns reported in Figure 5(c) revealedthe superior crystalline properties and tetragonal crystal phase of Sr_2FeMoO_6 nanorods. HRTEM was used to further analyze the atomic structure of the Sr_2FeMoO_6 nanorods (Figure 5(d)). Flawless single-crystal structures were verified through the observation of distinct lattice fringes. The interplanar spacings between horizontally and vertically adjacent lattice planes were 0.278 nm and 0.321 nm, respectively, in close agreement with the d-spacing values of the (010) planes (0.279 nm) and (102) planes (0.322 nm) of Sr_2FeMoO_6 [19, 20]

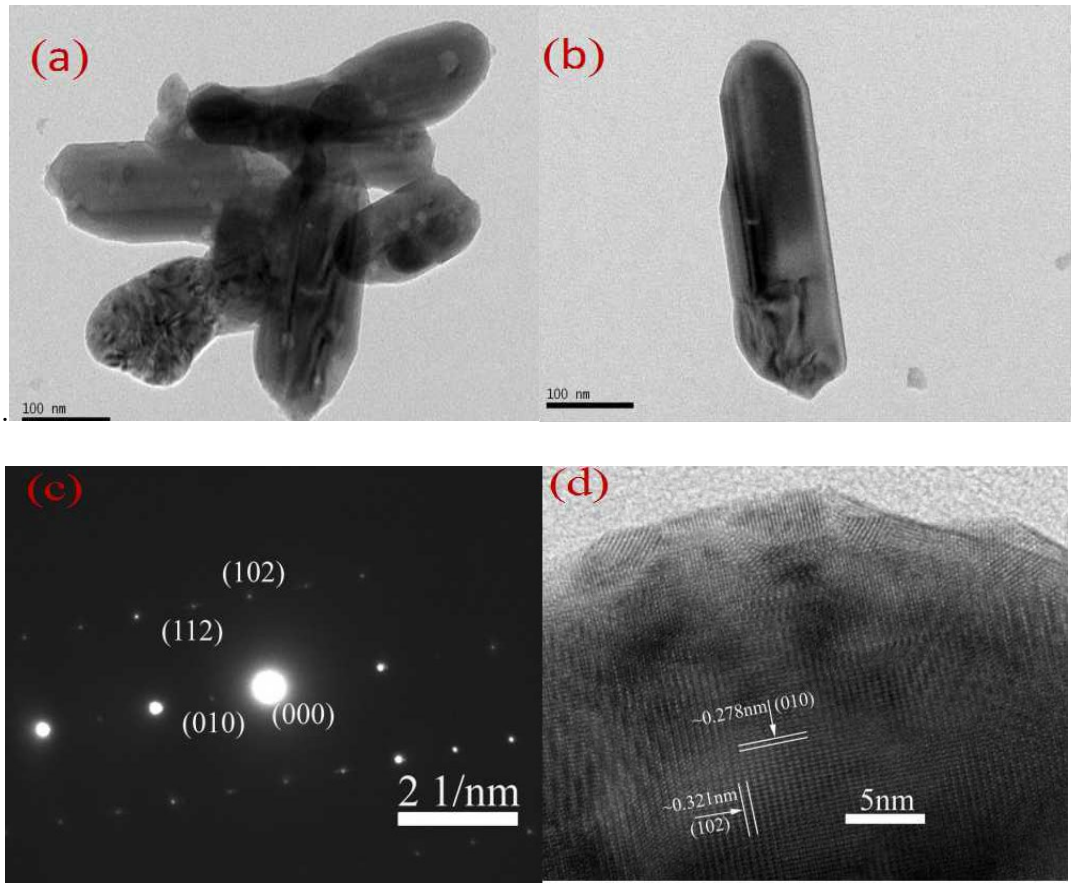

Fig.5. Microstructure characteristic of Sr_2FeMoO_6 sample: (a) (b) TEM image, (c) SAED pattern, (d) HRTEM image.

3.6. BET analysis

Figure 6 displays a typical N_2 adsorption-desorption isotherm of the Sr_2FeMoO_6 sample. The plot shows the rapid desorption and adsorption processes under high relative pressure and the

adsorption when P/P_0 approached 1.0. The measurements confirmed the presence of non-uniform pore structures within Sr_2FeMoO_6. Based on Brunauer-Emmett-Teller (BET) investigations, a specific surface area of 45.913m^2/g was calculated for Sr_2FeMoO_6. The large specific surface area can allow for strong adsorption, which is beneficial for the photocatalytic process as described below [21].

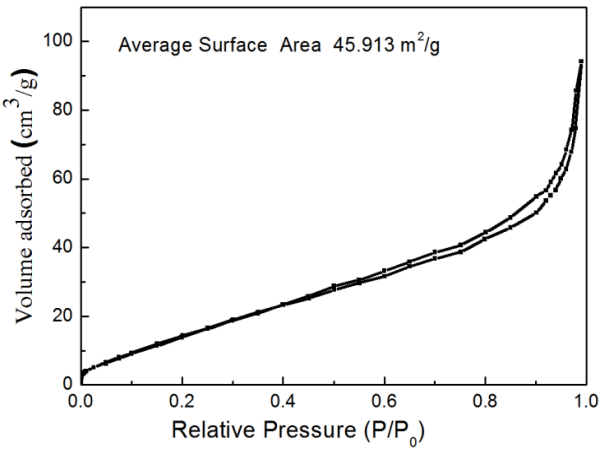

Fig.6. N_2 adsorption-desorption isotherms of Sr_2FeMoO_6 sample.

3.7. Optical properties

Figure 7 shows the diffuse reflectance spectrum of Sr_2FeMoO_6 sample at room temperature in the range of 200-800 nm, exhibiting absorption bands in the ultraviolet and visible region. The strong band observed at 250-450 nm was attributed to the absorption in molybdenum due to the charge transition between Mo^{6+}-O^{2-} [22].

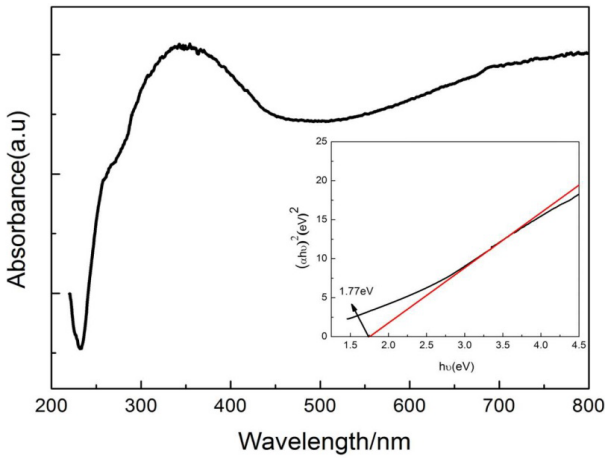

Fig.7. Diffuse-reflectance spectrum of Sr_2FeMoO_6 sample, the inset is the curve of $(\alpha hv)^2$ over hv.

In contrast, the absorption band between 500 and 800 nm was attributed to the electronic transitions corresponding to the d-d orbitals of Fe^{3+}. Alternatively, this absorption band may also be influenced by the transition involving ion interactions, such as the transformation from Fe^{3+} and Fe^{2+} to Fe^{4+} and Fe^{2+} [23, 24].

The reflectance spectrum can be used to evaluate the optical bandgap (Eg), which is closely related to light absorption through the formula: $\alpha h\upsilon = A(h\upsilon - Eg)^n$, where $h\upsilon$ is the incident photon energy, A is a proportional constant, Eg is the bandgap energy, and the value of n is related to the type of material. For n=1/2, Eg can be obtained by intercepting the linear part of $h\upsilon$ with abscissa coordinates by the epitaxy $(\alpha h\upsilon)^2$, resulting in an Eg of 1.77 eV. The bandgap is sufficiently narrow to overlap with a sizeable fraction of the visible spectrum, which is beneficial to photocatalytic activity, as confirmed by the following photocatalytic investigation [25].

3.8. Photocatalytic properties

Room-temperature degradation of the organic dye MB under visible-light irradiation was used to assess the photocatalytic performance of the synthesized Sr_2FeMoO_6 samples. Figure 8 displays the time evolution of the MB absorption spectrum when the reaction mixture was exposed to visible light. As the irradiation time increased, the intensity of the characteristic MB absorption peak at 664 nm gradually decreased.

In addition, a control experiment degrading MB without a photocatalyst was also conducted. Figure 9(a) indicates that approximately 10% of MB was degraded under visible-light irradiation for 35 min in the absence of a photocatalyst. The control experiment revealed that photo-induced self-sensitized photodegradation had almost no effect on MB, and the efficiency of dye degradation was the lowest in the given time. Conversely, when Sr_2FeMoO_6 was present, MB degradation approached 95.6% within 35 min of light irradiation. The determination of the degradation rate constant, designated as K_{app}, within the context of photocatalytic processes, can be achieved through the application of the pseudo-first-order rate equation $\ln(C_0 / C) = K_{app}t$, where C_0 is the initial MB concentration and C is the MB concentrations at irradiation time t [26]. As shown in Figure 9(b), the relationship between $\ln(C_0 / C)$ and irradiation time exhibited a good linear fit, indicating that the photocatalytic degradation process of MB follows pseudo-first-order kinetics. K_{app} of the Sr_2FeMoO_6 sample was determined as 0.08614 min^{-1}.

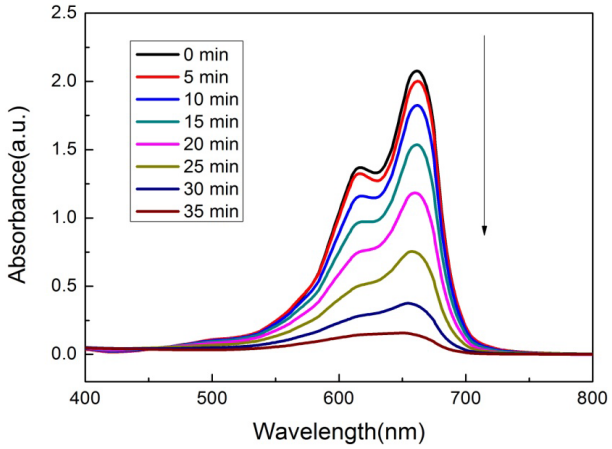

Fig.8. Absorption spectra of MB with irradiation time in the presence of Sr_2FeMoO_6 sample.

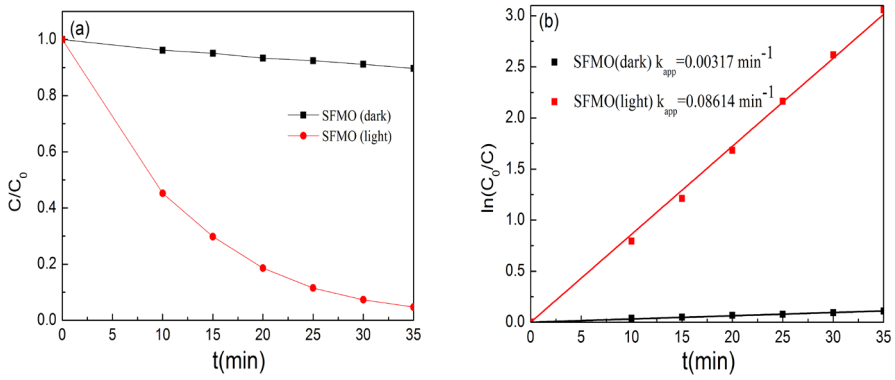

Fig.9. Plots of the photodegradation of MB by Sr_2FeMoO_6 sample: (a) C/C_0 over time; (b) $ln(C_0/C)$ over time.

The repeatability of the photocatalytic reaction and the lifetime of a photocatalyst are important parameters in any catalytic process, so it is essential to evaluate the stability of the catalyst and the reproducibility of the catalytic performance for practical application. Here, to assess the deactivation of the Sr_2FeMoO_6 sample, a series of recycling activity experiments were performed in five trials, and the result of this assessment is illustrated in Figure 10. The MB degradation efficiency (D_e) was 95.5%, 95.6%, 95.4%, 95.5%, and 95.4% over the five subsequent cycles. The result indicated that the prepared Sr_2FeMoO_6 sample has good reproducibility in the reaction process, implying that this double perovskite material can be applied as a photocatalyst in dye degradation.

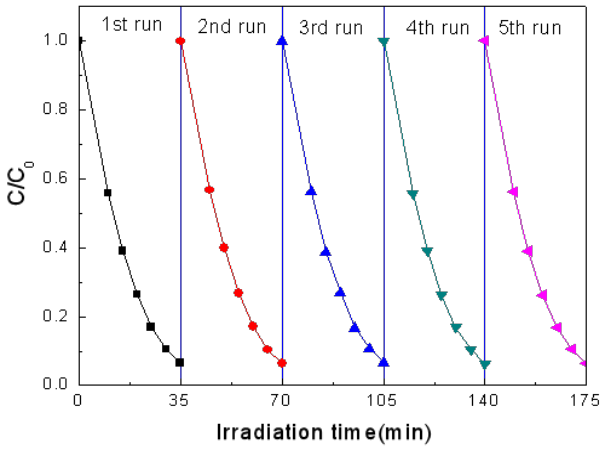

Fig.10. Photocatalytic cycle diagram of Sr_2FeMoO_6 sample.

3.9. ESR analysis

To further investigate the presence of free radicals in the reaction, the active oxygen species generated on the catalyst surface under simulated sunlight were detected by ESR technology. In the dark, no ESR signal was detected. Furthermore, no ESR signals of DMPO-·O_2^- were observed in the presence of Sr_2FeMoO_6 under light irradiation, indicating that the contribution of ·O_2^- in the oxidative mechanism is not dominant. However, four strong characteristic signals of the DMPO-·OH adduct were observed, suggesting that ·OH is another active species over Sr_2FeMoO_6. As mentioned in our previous article, surface-adsorbed oxygen vacancies function as electron acceptors, sequestering captured photo-induced electrons and thereby diminishing the surface recombination of electrons and holes. The captured photogenerated electrons can attack H_2O molecules to produce hydroxyl radicals (·OH). As a result, an increased a mount of photogenerated electrons is available to degrade the MB molecules, and the photodegradation rate is consequently enhanced [27, 28].

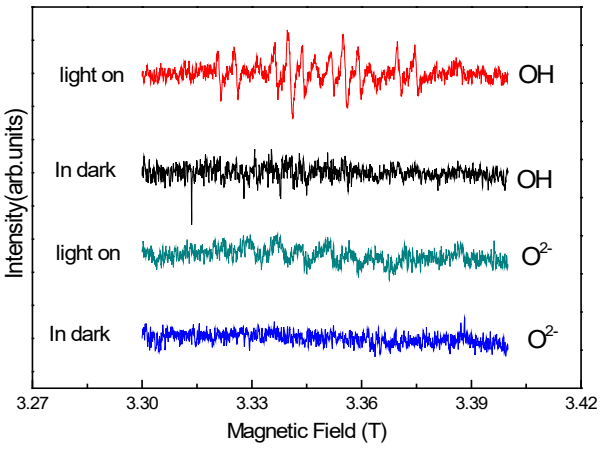

Fig.11. ESR signals of Sr_2FeMoO_6 sample.

4. Conclusions

Photocatalytic Sr_2FeMoO_6 double perovskite materials were synthesized by an improved sol-gel method. The structure, morphology, and optical properties were systematically and in-depth studied by TGA, XRD, Raman spectroscopy, SEM, HRTEM, and UV-vis spectroscopy. The photocatalytic degradation of MB was achieved with an efficiency of 95.6% in 35 min. This high photocatalytic performance is attributed to the following reasons: 1) the large surface area, which is beneficial for enhancing the adsorption of MB, thereby facilitating the photocatalytic process; 2) a narrow bandgap of 1.77 eV, which is very low when compared with usual photocatalysts such as TiO_2, allowing more photoelectrons to move from the valence band to the conduction band to significantly improve photocatalytic efficiency.

Acknowledgments

This work was financially supported by the Talent Scientific Research Foundation of Hefei University (21-22RC36) and the Higher Educational Natural Science Foundation of Anhui Province (2022AH051796)

References

[1] Z. Ghorbani, M. H. Ehsani, Ceramics International, 49, 27362(2023); https://doi.org/10.1016/j.ceramint.2023.06.001

[2] J. Hwang, R. R. Rao, L. Giordano,Y. Katayama, Y. Yu, Y. ShaoHorn, Science, 358, 751 (2017); https://doi.org/10.1126/science.aam7092

[3] F. A. Najar, K. Sultan, Journal of Physics and Chemistry of Solids, 171, 111039(2022); https://doi.org/10.1016/j.jpcs.2022.111039

[4] C. Bartha, C. Plapcianu, A. Crisan, M. Enculescu, A. Leca, Digest Journal of Nanomaterials and Biostructures, 11, 773(2016)

[5] A. S. Elyacoubi, R. Masrour, A. Jabar, M. Ellouze, E. K. Hlil, Materials Research Bulletin, 99, 132(2017); https://doi.org/10.1016/j.materresbull.2017.10.037

[6] L. Xu, C. X. Qin, Y. P. Wan, H. D. Xie, Y. L. Huang, L. Qin, H. J. Seo, Journal of the Taiwan Institute of Chemical Engineers, 71, 433(2017); https://doi.org/10.1016/j.jtice.2016.11.034

[7] V. R. Galakhov, E. Z. Kurmaev, K. Kuepper, M. Neumann, J. A. McLeod, A. Moewes, I. A. Leonidov, V. L. Kozhenikov, Journal of Physical Chemistry C, 114, 5154(2010); https://doi.org/10.1021/jp909091s

[8] M. Saloaro, M. Hoffmann, W. A. Adeagbo, S. Granroth, H. Deniz, H. Palonen, H. Huhtinen, S. Majumdar, P. Laukkanen, W. Hergert, A. Ernst, P. Paturi, ACS Applied Materials & Interfaces, 8, 20440(2016); https://doi.org/10.1021/acsami.6b04132

[9] L. Tan, Z. Q. Jiang, Y. Gao, S. G. Zhang, International Journal of Hydrogen Energy, 47, 20016(2022); https://doi.org/10.1016/j.ijhydene.2022.04.086

[10] T. Hatakeyama, S. Takeda, F. Ishikawa, A. Ohmura, A. Nakayama, Y. Yamada, A. Matsushita, J. Yea. Journal of the Ceramic Society of Japan, 118, 91(2010);

https://doi.org/10.2109/jcersj2.118.91

[11] M. Cernea, F. Vasiliu, C. Bartha, C. Plapcianu, M. Mercioniu, Ceramics International, 40, 11601(2014); https://doi.org/10.1016/j.ceramint.2014.03.142

[12] K. Hayat, K. S. Imran, Industrial & Engineering Chemistry Research, 55, 6619(2016)

[13] Y. Markandeya, Y. S. Reddy, S. Bale, G. Bhikshamaiah, Journal of Materials Science-Materials in Electronics, 29, 6711(2018); https://doi.org/10.1007/s10854-018-8657-4

[14] M. Cernea, F. Vasiliu, C. Plapcianu, C. Bartha, I. Mercioniu, I. Pasuk, R. Lowndes, R. Trusca, G. V. Aldica, L. Pintilie, Journal of the European Ceramic Society, 33, 2483(2013); https://doi.org/10.1016/j.jeurceramsoc.2013.03.026

[15] N. Kalanda, S. Demyanov, M. Krupa, S. M. Konoplyuk, Physica Status Solidi (B), 259, 2200021(2022); https://doi.org/10.1002/pssb.202200021

[16] T. Zhang, W. R. Branford, H. J. Trodahl, A. Sharma, J. Rager, J. L. MacManus-Driscoll, L. F. Cohen, Journal of Raman Spectroscopy, 35, 1081(2004); https://doi.org/10.1002/jrs.1258

[17] E. Yadav, G. L. Prajapati, P. Rajput, K. R. Mavani, New Journal of Physics, 25, 123044 (2023); https://doi.org/10.1088/1367-2630/ad121c

[18] L. H. Zheng, C. Liu, Z. B. Xu, Z. Y. Zheng, Y. Wang, T. Wang, Applied Physics A: Materials Science & Processing, 127, 250(2021)

[19] Q. Zhang, Y. X. Tang, J. Liang, S. H. Gao, Journal of Alloys and Compounds, 976, 173078 (2024); https://doi.org/10.1016/j.jallcom.2023.173078

[20] Z. Ghorbani, M. H. Ehsani, Physica B, 682, 415867(2024); https://doi.org/10.1016/j.physb.2024.415867

[21] Y. Alizad Farzin, A. Babaei, A. Ataie, Ceramics International, 46, 16867(2020); https://doi.org/10.1016/j.ceramint.2020.03.264

[22] N. Xiao, J. Shen, T. Xiao, B. Xu, X. Luo, L. Li, Z. Wang, X. Zhou Materials Research Bulletin, 70, 684(2015); https://doi.org/10.1016/j.materresbull.2015.06.001

[23] H. Wu, Y. Ma, Y. Qian, E. Kan, R. Lu, Y. Liu, W. Tan, C. Xiao, K. Deng, Solid State Communications, 177, 57(2014); https://doi.org/10.1016/j.ssc.2013.09.029

[24] D. Yang, T. Yang, Q. Sun, Y. Chen, G. I. Lampronti, Journal of Alloys and Compounds, 728, 337(2017); https://doi.org/10.1016/j.jallcom.2017.09.027

[25] S. Bhattacharjee, R. K. Parida, B. N. Parida, Physica B, 659, 414849 (2023); https://doi.org/10.1016/j.physb.2023.414849

[26] X. Xu, X. Ding, X. L. Yang, P. Wang, S. Li, Z. X. Lu, H. Chen, Journal of Hazardous Materials, 364, 691(2019); https://doi.org/10.1016/j.jhazmat.2018.10.063

[27] X. Y. Li, Z. F. Yao, L. Y. Zhang, G. H. Zheng, Z. X. Dai, K. Y. Chen, Applied Surface Science, 480, 262(2019); https://doi.org/10.1016/j.apsusc.2019.02.115

[28] Q. Zhang, Y. Huang, S. Q. Peng, T. T. Huang, J. J. Cao, W. K. Ho, S. C. Lee, Applied Catalysis B: Environmental, 239, 1(2018); https://doi.org/10.1016/j.apcatb.2018.07.076